

Choongho Yu¹
Sanjoy Saha
Jianhua Zhou
Li Shi²

Department of Mechanical Engineering
and Center for Nano and Molecular Science and
Technology,
Texas Materials Institute,
The University of Texas at Austin,
Austin, Texas 78712

Alan M. Cassell
Brett A. Cruden
Quoc Ngo
Jun Li

Center for Nanotechnology,
NASA Ames Research Center,
Moffett Field, CA 94035

Thermal Contact Resistance and Thermal Conductivity of a Carbon Nanofiber

We have measured the thermal resistance of a 152-nm-diameter carbon nanofiber before and after a platinum layer was deposited on the contacts between the nanofiber and the measurement device. The contact resistance was reduced by the platinum coating for about 9–13% of the total thermal resistance of the nanofiber sample before the platinum coating. At a temperature of 300 K, the axial thermal conductivity of the carbon nanofiber is about three times smaller than that of graphite fibers grown by pyrolysis of natural gas prior to high-temperature heat treatment, and increases with temperature in the temperature range between 150 K and 310 K. The phonon mean free path was found to be about 1.5 nm and approximately temperature-independent. This feature and the absence of a peak in the thermal conductivity curve indicate that phonon-boundary and phonon-defect scattering dominate over phonon-phonon Umklapp scattering for the temperature range. [DOI: 10.1115/1.2150833]

Keywords: contact resistance, nanofiber, thermal conductivity, uncertainty analysis, platinum coating, nanoscale contact, thermal constriction resistance, phonon scattering

Introduction

Diamond, graphite, and graphite fibers have been known as excellent heat conductors with a high thermal conductivity up to 3000 W/m-K [1–3]. Recently, the axial thermal conductivity of individual multiwalled carbon nanotubes (CNTs) [4] has been found to be higher than 3000 W/m-K at a temperature of 300 K [5]. It was also found that the effective thermal conductivity of CNT mats [6] and CNT bundles [7] was one or two orders of magnitude lower than that of individual defect-free CNTs due to the large thermal contact resistance between adjacent CNTs in the bundles.

It has been suggested that CNTs and carbon nanofibers (CNFs) can be used as thermal interface materials to enhance contact thermal conductance for electronic packaging applications. Several groups have reported mixed experimental results from no improvements to large improvements in the thermal contact conductance due to the CNTs and CNFs [8–12]. These mixed results can be caused by the difference in surface coverage and perpendicular alignment of the CNTs or CNFs. Moreover, the results can be affected by two other factors. First, the CNTs and CNFs grown using different methods possess different defect densities and different intrinsic thermal conductivities. Secondly, the contact thermal resistance of the nanometer scale point and line contacts between a CNT or CNF and a planar surface can be high due to enhanced phonon-boundary scattering at the nanocontacts.

We have used a microfabricated device to measure the thermal resistance of an individual CNF from a vertically aligned CNF film for applications as thermal interface materials. The measure-

ment was conducted before and after a platinum (Pt) layer was deposited on the contacts between the CNF and the microdevice so as to investigate the thermal contact resistance between the CNF and a planar surface. The contact resistance was reduced by the platinum coating for about 9–13% of the total thermal resistance of the nanofiber sample before the Pt coating. At temperature 300 K, the obtained axial thermal conductivity of the carbon nanofibers was about three times smaller than that of graphite fibers grown by pyrolysis of natural gas prior to high-temperature heat treatment.

Experimental Methods

Nanostructure Growth. CNFs were grown using a plasma-enhanced chemical vapor deposition (PECVD) method as described previously [13]. Briefly, silicon substrates with a predeposited 30-nm-thick Ti barrier layer and a 30-nm-thick Ni catalyst layer were subjected to a glow discharge at a dc bias of 585 V, 500 W, and 0.85 A under a total flow of 100 standard cubic centimeter per minute (sccm) of 4:1 NH₃:C₂H₂ process gas mixture at 4 Torr for 45 min. CNF growth rate under these conditions was approximately 500 nm/min. Cross-sectional transmission electron micrographs (Fig. 1) were obtained to investigate the CNF quality and graphitic microstructure. The CNFs possessed cone angles between 5°–20° with typical cone angles around 10° (Fig. 1(c)).

Measurement Procedure. The measurement was conducted with the use of a previously reported method based on a microdevice. A detailed description of the measurement method can be found in Ref. [7]. In brief, the microdevice consists of two symmetric silicon nitride (SiN_x) membranes suspended by long SiN_x beams, as shown in Fig. 2(a). A Pt serpentine line was patterned on each membrane and used as a heater and resistance thermometer (RT). A nanofiber deposited from a suspension was trapped between the two membranes. When a dc current (*I*) was supplied

¹Current address: Materials Sciences Division, Lawrence Berkeley National Laboratory, Berkeley, CA 94720.

²Author to whom correspondence should be addressed; e-mail: lishi@mail.utexas.edu

Contributed by the Heat Transfer Division of ASME for publication in the JOURNAL OF HEAT TRANSFER. Manuscript received December 20, 2004; final manuscript received September 18, 2005. Review conducted by C. P. Grigoropoulos.

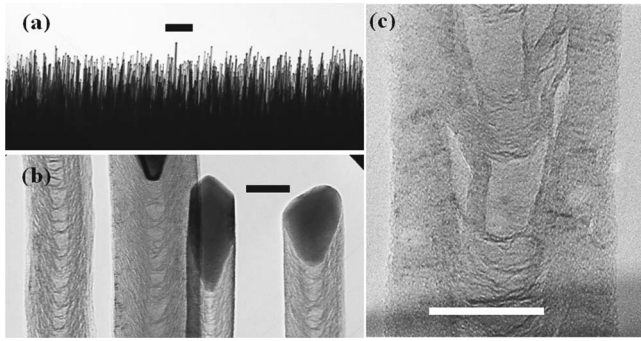


Fig. 1 Cross-sectional transmission electron micrographs of the as grown carbon nanofibers obtained from PECVD. Panel (a) shows a low magnification image depicting the vertical orientation and alignment of the carbon nanofibers. Panel (b) shows a higher magnification image which reveals the microstructural arrangement of the graphitic sheets in the fibers and panel (c) details the disordered crystalline morphology that reveals nanofiber cone angles around 10 deg. Scale bars are 2 μm , 50 nm, and 20 nm, respectively, for (a), (b), and (c).

to one Pt RT to raise the temperature of one membrane, part of the Joule heat generated in the heating membrane was conducted through the carbon nanofiber to the other (sensing) membrane.

The temperature distribution in each membrane can be assumed to be uniform compared to the average temperature rise in the membrane because the internal thermal resistance of the membrane is on the order of 10^5 K/W, which is two orders of magnitude smaller than either the sample thermal resistance or the thermal resistance of the five SiN_x beams. To verify the temperature uniformity, we have used a commercial finite element package (ANSYS) to calculate the three-dimensional (3D) temperature distribution in the measurement device. The top view of the calculated temperature distribution is shown in Fig. 3. For a device with ten supporting beams of the length $L=210$ μm , the maximum temperature difference in the heating (or sensing) membrane is 1.5% (or 6.5%) of the temperature rise in the membrane. For another design with $L=420$ μm , the maximum temperature difference in the heating (or sensing) membrane is 1.8% (or 3.1%) of the temperature rise in the membrane.

The two Pt RTs were used to measure the temperature rises on the heating and sensing membranes at different I values, i.e., $\Delta T_h(I) \equiv T_h(I) - T_h(I=0)$ and $\Delta T_s(I) \equiv T_s(I) - T_s(I=0)$, respec-

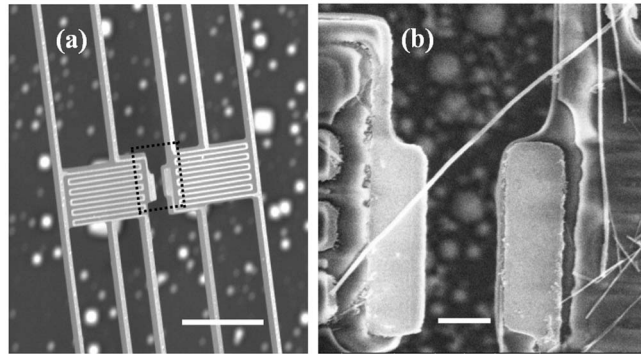


Fig. 2 (a) A scanning electron microscopy (SEM) image of the microdevice before the nanofiber was deposited. (b) A SEM image of a rectangular portion in (a) showing a carbon nanofiber bridging two membranes. The scale bars correspond to 20 μm and 2 μm , respectively, in (a) and (b).

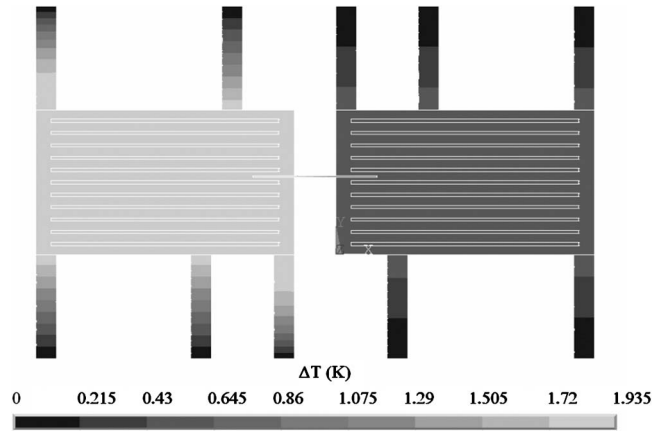


Fig. 3 Calculated temperature distribution in the measurement device. Each membrane is 25 μm long, 14 μm wide, and 0.5 μm thick. Each of the ten supporting beams of the actual device was 210 μm long and 2 μm wide. In the calculation, the beam length was scaled down to 10 μm with the thermal resistance of the beams kept the same by rescaling the thermal conductivity of the beams. The edges of the RTs and the nanowire are highlighted in white. The contact resistance per unit length between the nanofiber and the membrane was taken to be 0.03 Km/W.

tively. The thermal conductance (G_b) of the five beams supporting each membrane and the thermal conductance (G_m) of the sample were obtained as

$$G_b = \frac{Q_h + Q_L}{\Delta T_h + \Delta T_s} \quad (1a)$$

and

$$G_m = G_b \frac{\Delta T_s}{\Delta T_h - \Delta T_s} \quad (1b)$$

where Q_h is the Joule heat dissipation in the Pt RT on the heating membrane, and Q_L is the Joule heat dissipation in one of the two identical Pt leads supplying the dc heating current to the heating RT.

Data Processing and Uncertainty Analysis. The measurement uncertainty of this method was discussed previously for the case of a single point measurement at a fixed I value [7]. To improve the measurement uncertainty, we ramped I from zero to a negative maximum ($-I_{\text{max}}$), from $-I_{\text{max}}$ back to zero, from zero to a positive maximum (I_{max}), and from I_{max} back to zero. One ramping cycle took about 11 min. During each ramping cycle, a total number of $N=203$ sets of measurements were taken. G_b was obtained as the slope of a least-square linear curve fit of $Q \equiv (Q_h + Q_L)$ as a function of $(\Delta T_h + \Delta T_s)$ according to Eq. (1a), as illustrated in Fig. 4(a). The ratio G_m/G_b was then obtained as the slope of a linear curve fit of the measured ΔT_s as a function of the measured $(\Delta T_h - \Delta T_s)$ according to Eq. (1b), as shown in Fig. 4(b). G_m is then obtained as $G_m = G_b(G_m/G_b)$.

The uncertainty in each G_m measurement, i.e., U_{G_m} , was calculated from the uncertainties in G_b and G_m/G_b , i.e., U_{G_b} and U_{G_m/G_b} , according to

$$\frac{U_{G_m}}{G_m} = \sqrt{\left(\frac{U_{G_b}}{G_b}\right)^2 + \left(\frac{U_{G_m/G_b}}{G_m/G_b}\right)^2} \quad (2)$$

U_{G_b} and U_{G_m/G_b} were calculated as the uncertainties in the slope of the corresponding least-square linear fitting according to the error propagation method of Coleman and Steele [14]. Both random and systematic errors in individual (X_i, Y_i) data set were

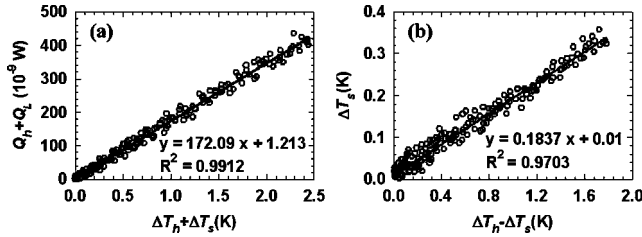


Fig. 4 (a) Measurement results of $Q_h + Q_L$ plotted as a function of $\Delta T_h + \Delta T_s$; (b) Measurement results of ΔT_s plotted as a function of $\Delta T_h - \Delta T_s$. Also shown in each figure are the equation and the square of the Pearson product moment correlation coefficient (R^2) of the linear curve fitting.

accounted for by this method.

During each ramping cycle of the measurement, four (X_i, Y_i) data sets were measured at the same I magnitude. The random uncertainties in Y_i and X_i are calculated as $P_{Y_i} = t_{v,95} S_{Y_i}$ and $P_{X_i} = t_{v,95} S_{X_i}$, where $t_{v,95} = 3.182$ is the t distribution for a $v = 3$ degrees of freedom corresponding to a sample size of four at a confidence level of 95%, and S_{Y_i} (or S_{X_i}) is the sample standard deviation of the four Y_i (or X_i) measurement results at the same I magnitude.

As discussed by Brown et al. [15], systematic errors that are a fixed value or “percent of full scale” have no influence on the uncertainty of the slope and thus do not need to be accounted for. On the other hand, a systematic error of a second type that is a function of the magnitude of the variables, such as those of a “percent of reading” nature, can cause a nonzero systematic uncertainty in the slope of the linear curve fit. This second type of systematic errors in the measurement results of ΔT_h , ΔT_s , Q_L , and Q_h were identified and calculated as following.

First, the Pt RT was calibrated with one of the two factory-calibrated silicon diodes in the cryostat serving as the reference temperature (T_r). The specified uncertainty of T_r is $U_{T_r} = 0.01\% T_r$, including both random and systematic errors. Due to a small temperature gradient in the cryostat, there was a less than 0.2% difference between the temperature readings of the two diodes that were located 4.5 cm apart from each other. The RT on the microdevice was located between the two diodes and the diode right next to the RT was used as the reference in the temperature calibration. The difference between T_r and the actual temperature of the RT should be less than 0.2% because the distance between the RT and the reference diode was much shorter than that between the two diodes. Thus, the systematic error in the calibration of the RT was calculated to be $B_T \leq 0.2\% T$. Because $B_{T_h(I)}$ and $B_{T_h(I=0)}$ arise from the same calibration error and are thus perfectly correlated, the propagation of $B_{T_h(I)} \leq 0.2\% T_h(I)$ and $B_{T_h(I=0)} \leq 0.2\% T_h(I=0)$ results in $B_{\Delta T_h(I)} \leq 0.2\% \Delta T_h(I)$ [14]. In other words, because $T_h(I)$ and $T_h(I=0)$ were distorted by the same percent of the reading due to the same calibration error, $\Delta T_h(I)$ was distorted by the same percent of the reading. Similarly, $B_{\Delta T_s(I)} \leq 0.2\% \Delta T_s(I)$. Because T_h and T_s were calibrated using the same T_r and thus B_{T_h} and B_{T_s} arise from the same calibration error, B_{T_h} and B_{T_s} are also perfectly correlated and propagate into $B_{(\Delta T_h - \Delta T_s)} \leq 0.2\% (\Delta T_h - \Delta T_s)$ and $B_{(\Delta T_h + \Delta T_s)} \leq 0.2\% (\Delta T_h + \Delta T_s)$.

The Joule heat Q was obtained as a product of the measured voltage (V) and current (I). The systematic error of the second type in the V measurement, i.e., B_V , was specified in the instrument manual to be less than 0.05% of the reading, and this error (B_I) in the I measurement was less than 0.1% of the reading. Hence, the same type of error in Q was calculated as $B_Q = (B_I^2/I^2 + B_V^2/V^2)^{1/2} Q = 0.125\% Q$.

The dominant uncertainty source is the random fluctuation in

the temperature measurement. This fluctuation was observed to be about 40×10^{-3} K, as evident in Fig. 4(b). The random fluctuation was caused by the temperature fluctuation of the evaluated cryostat where the sample was located as well as the random uncertainty of the lock-in amplifier that was used to measure the differential electrical resistance of the RT. The uncertainty calculation shows that the random uncertainty accounts for more than 95% of U_{G_m} .

To reduce the uncertainty, for each measurement we often needed to spend a few hours to reduce the temperature fluctuation of the cryostat and used a sufficiently large ΔT_h value of about 2 K to obtain U_{G_m}/G_m between 4% and 15%. In addition, we obtained three to seven measurement results with $U_{G_m}/G_m \leq 15\%$ at one temperature, and the averaged value ($\overline{G_m}$) of the several G_m results is reported because the random uncertainty is reduced with increasing number (n) of measurements. The total uncertainty in $\overline{G_m}$ is calculated as

$$U_{\overline{G_m}} = (P_{\overline{G_m}}^2 + B_{\overline{G_m}}^2)^{1/2} \quad (3)$$

where the random uncertainty in $\overline{G_m}$ is calculated as

$$P_{\overline{G_m}} = t_{n-1,95} S_{G_m} / \sqrt{n} \quad (4)$$

where S_{G_m} is the sample standard deviation of the n measurements of G_m , and $t_{n-1,95}$ is the t distribution for $n-1$ degree of freedom and a confidence level of 95%.

In Eq. (3), $B_{\overline{G_m}}$ is the systematic error of the second type in $\overline{G_m}$. Because B_{G_m}/G_m is the same for each measurement, $B_{\overline{G_m}}/\overline{G_m} = B_{G_m}/G_m$. In the fitting to obtain G_m/G_b , $B_{(\Delta T_h - \Delta T_s)}$ and $B_{\Delta T_s}$ are perfectly correlated because they share the same error source. In other words, the obtained X and Y variables in Fig. 4(b) were distorted by the same percent of the reading, or $B_{(\Delta T_h - \Delta T_s)}/(\Delta T_h - \Delta T_s) = B_{\Delta T_s}/\Delta T_s$. Consequently, the slope G_m/G_b is not affected by this perfectly correlated error, resulting in $B_{G_m/G_b} = 0$. Therefore, $B_{\overline{G_m}}/G_m = \sqrt{(B_{G_b}/G_b)^2 + (B_{G_m}/G_b)/(G_m/G_b)^2} = B_{G_b}/G_b$. In the fitting step for obtaining G_b , $B_{(\Delta T_h + \Delta T_s)}$ and B_Q are not correlated. Thus

$$\frac{B_{\overline{G_m}}}{\overline{G_m}} = \frac{B_{G_m}}{G_m} = \frac{B_{G_b}}{G_b} = \sqrt{\left(\frac{B_{(\Delta T_h + \Delta T_s)}}{\Delta T_h + \Delta T_s}\right)^2 + \left(\frac{B_Q}{Q}\right)^2} \leq 0.24\% \quad (5)$$

Reduction of the Thermal Contact Resistance. The measured thermal resistance of the sample ($R_m = G_m^{-1}$) consists of the intrinsic thermal resistance of the nanofiber (R_n) and the total contact thermal resistance between the nanofiber and the two membranes (R_c), i.e.,

$$R_m = R_n + R_c \quad (6)$$

To reduce R_c , we used a focused electron beam deposition method to deposit a thin Pt layer locally on the contacts from precursor gases in a dual beam focused ion beam (FIB) tool. The deposited Pt layer is shown in Figs. 5(a) and 5(b). The effective contact area between the nanofiber and the membranes was increased by the Pt layer.

Measurement Results and Discussions

Figure 6 shows the measured thermal resistance (R_m) before and after the Pt coating on the contacts. The difference in R_m is caused by the reduction in the thermal contact resistance by the Pt layer, and the reduction of the contact resistance (R_c), i.e., ΔR_c , is shown in the inset of Fig. 6. The uncertainty in ΔR_c is calculated as the root-sum-square of the uncertainty in R_m before the Pt coating and that after the Pt coating. The contact resistance was reduced by the Pt coating for about 9–13% of the R_m value obtained before the Pt coating.

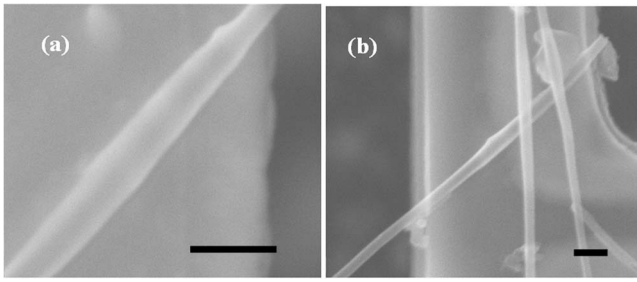


Fig. 5 SEM images of the two contacts between the nanofiber and the two membranes after a thin Pt layer was deposited on the contacts. The scale bars in the two images are 500 nm.

We have calculated the contact resistance using an approach based in part on a recent work by Bahadur et al. [16], who have extended McGee et al.'s model [17] of the thermal resistance of cylinder-flat contacts to analyze the constriction thermal resistance (R'_c) of unit contact length between a nanowire and a flat surface. The contact width ($2b$) between the cylinder and the surface can be calculated from the contact force.

Bahadur et al. calculated the contact force between a nanowire and a substrate to be the van der Waals force. The calculation requires the knowledge of the Hamaker constant (A) that can be calculated from Lifshitz-van der Waals coefficient [18]. For the contact between Pt and carbon (C) in vacuum, the Hamaker constant can be estimated from those of Pt-Pt and C-C interfaces to be $A_{Pt-C} \approx \sqrt{A_{Pt-Pt}A_{C-C}}$ [18,19]. We could not find the Hamaker constant for Pt-Pt and graphite-graphite interfaces in the literature, and have used the values for Au-Au and diamond-diamond interfaces to approximate A_{Pt-Pt} and A_{C-C} and obtained $A_{Pt-C} \approx 4 \times 10^{-19}$ J for the contact between the nanofiber and the membrane. In the calculation, we have used Van der Waals radii for Pt and carbon found in Ref. [20]. Based on these alternative properties, we calculated that the contact width ($2b$) between the 152-nm-diameter nanofiber and the Pt surface was approximately 10 nm.

Because the temperature of the nanofiber segment in contact with the membrane varies along the nanofiber as a result of heat transfer to the membrane, the portion of the nanofiber in contact with the membrane should be treated as a fin. The thermal contact resistance between the nanofiber and the sensing membrane is thus the fin resistance. Assuming adiabatic boundary condition at

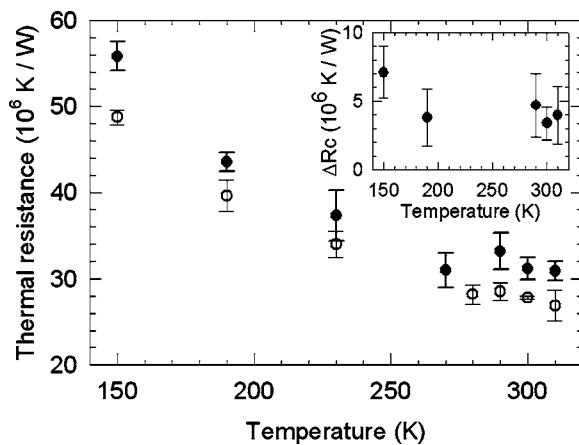


Fig. 6 Measured thermal resistance of the nanofiber sample before a Pt layer was deposited (solid black circles) and after a Pt layer was deposited with the use of the electron beam (open circles). The inset shows the reduction in contact resistance, ΔR_c , after the Pt coating.

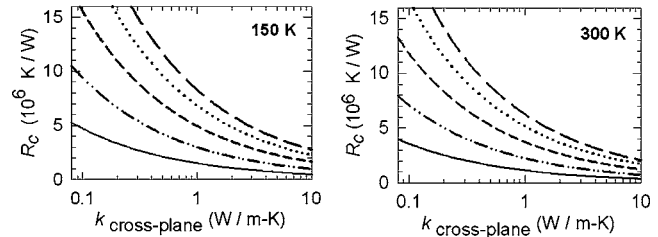


Fig. 7 Calculation results of thermal contact resistance (R_c) at 150 K and 300 K as a function of the cross-plane thermal conductivity (k_{\perp} or $k_{\text{cross-plane}}$) of the nanofiber. The five lines in each figure correspond to a contact width of $2b=0.1$ nm (long dashed line), $2b=1$ nm (dotted line), $2b=10$ nm (short dashed line), $2b=50$ nm (double dotted line), and $2b=100$ nm (solid line).

the end of the nanofiber fin, the total thermal contact resistance of the two contacts between the nanofiber and the two membranes can be calculated as [2]

$$R_c = \frac{2}{\sqrt{\frac{k_{\parallel} \pi D^2}{4R'_c} \tanh\left(l \sqrt{\frac{4}{k_{\parallel} \pi D^2 R'_c}}\right)}} \quad (7)$$

where k_{\parallel} is the axial thermal conductivity of the nanofiber, and l_c is the contact length in the axial direction. The radial or cross-plane thermal conductivity of the nanofiber, i.e., k_{\perp} , is needed for the calculation of R'_c . Although the cross-plane thermal conductivity of graphite is given in the literature to be $k_{\perp}=5.7$ W/m-K at 300 K [2], the value for the nanofiber can be different because of different crystalline structure and quality. More importantly, the effective thermal conductivity at a point contact of a Knudsen number (K) of the order of unity or larger, where K is the ratio between the phonon mean free path and the contact width, can be substantially reduced [21]. This reduction needs to be taken into account in the calculation of the contact resistance based on the continuum model when the contact width is comparable to or smaller than the mean free path. On the other hand, the axial or in-plane thermal conductivity k_{\parallel} can be calculated from the measured thermal resistance of the nanofiber after the Pt coating. Using the obtained k_{\parallel} values at 150 K and 300 K, we have calculated the contact thermal resistance as a function of k_{\perp} for different contact widths of $2b=0.1$ nm, 1 nm, 10 nm, 50 nm, and 100 nm. The results are shown in Fig. 7.

Without the Pt coating, a contact width of $2b=50$ and 100 nm is rather unlikely because the diameter of the nanofiber is only 152 nm. With the Pt coating, on the other hand, a contact width of $2b \geq 50$ nm is possible. If $2b \geq 50$ nm with the Pt coating and $2b \approx 10$ nm without the Pt coating, the calculated ΔR_c can match the measurement value when $k_{\perp} < 0.6$ W/m-K for 150 K and $k_{\perp} < 2$ W/m-K for 300 K. For this case, the residual R_c after the Pt coating is comparable to the measure ΔR_c shown in the inset of Fig. 6.

We have used the thermal resistance results measured after the Pt coating to calculate the axial thermal conductivity of the nanofiber. The results are shown in Fig. 8. As a comparison, Fig. 8 also shows the measured thermal conductivity of a graphite fiber grown by pyrolysis prior to heat treatment. The thermal conductivity of the PECVD nanofiber increases nearly linearly with the temperature in the temperature range between 150 K and 310 K and the value at 300 K is about three times smaller than that of the graphite fiber. Note that the thermal conductivity of the graphite fiber and the specific heat (C) of graphite [22] increase nearly linearly with temperature in the temperature range between 150 K and 310 K. Using the specific heat of graphite and a sound velocity of $v=10000$ m/s, we have calculated the phonon mean free path (l) according to the thermal conductivity formula, i.e., k

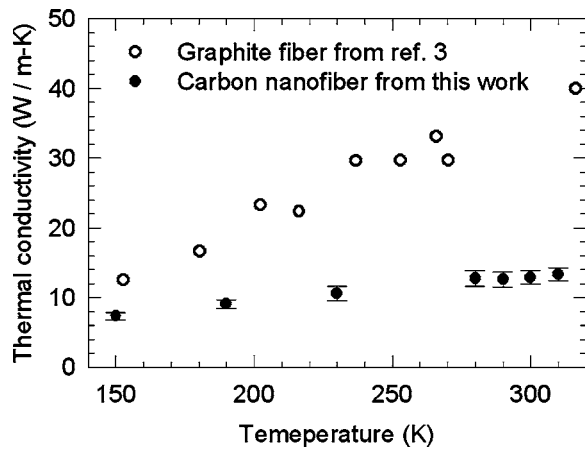


Fig. 8 Thermal conductivity of the nanofiber (solid circles) calculated from the measured thermal resistance of the sample after the Pt coating. The uncertainty error bars do not include the residual contact resistance after the Pt coatings. The thermal conductivity of a graphite fiber (open circles) from Ref. [3] is shown for comparison.

$=Cv/l^3$. The obtained mean free path of $l \approx 1.5$ nm is almost independent of temperature between 150 K and 310 K. This feature and the absence of a peak in the thermal conductivity curve indicates that phonon-boundary and phonon-defect scattering with a short mean free path dominates over phonon-phonon Umklapp scattering for the temperature range. The short mean free path indicates that there is a high density of defects in the nanofiber.

Conclusion

We have measured the thermal resistance of a 152-nm-diameter carbon nanofiber grown by using PECVD before and after a platinum layer was deposited on the contacts between the nanofiber and the measurement device. The contact resistance was reduced by the Pt coating for about 9–13% of the total thermal resistance before the Pt coating. The in-plane thermal conductivity of the carbon nanofiber increases with temperature in the temperature range between 150 K and 310 K, and the value at 300 K was about three times smaller than that of graphite fibers grown by pyrolysis of natural gas prior to high-temperature heat treatment. The phonon mean free path in the nanofiber was found to be about 1.5 nm and is independent of temperature. This feature and the absence of a peak in the thermal conductivity curve indicate that phonon-boundary and phonon-defect scattering dominates over phonon-phonon Umklapp scattering for the temperature range. To develop thermal interface materials using CNT or CNF films, it is necessary to reduce the defect density and increase the intrinsic thermal conductivity of the carbon nanostructures. Additionally, the contact thermal resistance at the nanoscale point or line contacts between CNTs and the surrounding should not be underestimated.

Acknowledgment

Four of the authors (C.Y., S.S., J.Z., L.S.) were supported by the Chemical and Transport System Division of the National Science Foundation and by SEMATECH through the Advanced Materials Research Center (AMRC).

Nomenclature

- A = Hamaker constant (N/m)
- b = half width of the contact line between the nanofiber and the substrate (m)
- B_x = systematic or bias uncertainty for the x variable

- D = diameter of the nanofiber (m)
- G_m = measured thermal conductance of the sample (W/K)
- G_b = thermal conductance of the five beams of one membrane (W/K)
- I = dc current (A)
- k_n = thermal conductivity of the nanofiber (W/m-K)
- k_s = thermal conductivity of the substrate (W/m-K)
- k_{\parallel} = in-plane or axial thermal conductivity (W/m-K)
- k_{\perp} = cross-plane or radial thermal conductivity (W/m-K)
- l_c = contact length along the axis of the nanofiber (m)
- l_i = length of the Pt layer deposited on the nanofiber along the axis of the nanofiber (m)
- L = length of a SiN_x beam of the measurement device (m)
- P_x = random or precision uncertainty for the x variable
- Q_h = Joule heat dissipation in the Platinum resistance thermometer (W)
- Q_L = Joule heat dissipation in one of the two Pt leads supplying the dc current (I) to the heating Pt RT (W)
- R = thermal resistance (K/W)
- R_c = thermal contact resistance between the nanofiber and the two membranes (K/W)
- R'_c = constriction thermal resistance of unit axial length of the nanofiber (K m/W)
- R_m = measured thermal resistance (K/W)
- R_n = intrinsic thermal resistance of the nanofiber (K/W)
- T = temperature (K)
- T_h = temperature of the heating membrane (K)
- T_s = temperature of the sensing membrane (K)
- T_r = reference temperature in temperature calibration (K)
- U_x = uncertainty for the x variable

References

- [1] Touloukian, Y. S., Powell, R. W., Ho, C. Y., and Klemens, P. G., 1970, *Thermal Conductivity: Nonmetallic Solid, Thermophysical Properties of Matter*, Plenum, NY, Vol. 2.
- [2] Incropera, F. P., and Dewitt, D. P., 1996, *Fundamentals of Heat and Mass Transfer*, Wiley, NY.
- [3] Heremans, J., and Beetz, C. P. Jr., 1985, "Thermal Conductivity and Thermopower of Vapor-grown Graphite Fibers," *Phys. Rev. B*, **32**, pp. 1981–1986.
- [4] Dresselhaus, M. S., Dresselhaus, G., and Eklund, P. C., 1996, *Science of Fullerenes and Carbon Nanotubes*, Academic, New York.
- [5] Kim, P., Shi, L., Majumdar, A., and McEuen, P. L., 2001, "Thermal Transport Measurements of Individual Multiwalled Carbon Nanotubes," *Phys. Rev. Lett.*, **87**, pp. 215502(1-4).
- [6] Hone, J., Llaguno, M. C., Nemes, N. M., and Johnson, A. T., Fischer, J. E., Walters, D. A., Casavant, M. J., Schmidt, J., and Smalley, R. E., 2000, "Electrical and Thermal Transport Properties of Magnetically Aligned Single Wall Carbon Nanotube Films," *Appl. Phys. Lett.*, **77**(5), pp. 666–668.
- [7] Shi, L., Li, D., Yu, C., Jang, W., Yao, Z., Kim, P., and Majumdar, A., 2003, "Measuring Thermal and Thermoelectric Properties of One-Dimensional Nanostructures Using a Microfabricated Device," *J. Heat Transfer*, **125**, pp. 881–888.
- [8] Chuang, H. F., Cooper, S. M., Meyyappan, M., and Cruden, B. A., 2004, "Improvement of Thermal Contact Resistance by Carbon Nanotubes and Nanofibers," *J. Nanosci. Nanotechnol.*, **4**(8), pp. 964–967.
- [9] Ngo, Q., Cruden, B. A., Cassell, A. M., Walker, M. D., Ye, Q., Koehne, J. E., Meyyappan, M., Li, J., and Yang, C. Y., 2004, "Thermal Conductivity of Carbon Nanotube Composite Films," *Mater. Res. Soc. Symp. Proc.*, **812**, F3.18.1–6.
- [10] Ngo, Q., Cruden, B. A., Cassell, A. M., Sims, G., Meyyappan, M., Li, J., and Yang, C. Y., 2004, "Thermal Interface Properties of Cu-filled Vertically Aligned Carbon Nanofiber Arrays," *Nano Lett.*, **4**(12), pp. 2403–2407.
- [11] Xu, J., and Fisher, T. S., 2004, "Enhanced Thermal Contact Conductance using Carbon Nanotube Arrays," *The Ninth Intersociety Conference on Thermal and Thermomechanical Phenomena in Electronic Systems, ITherm'04*, **2**, pp. 549–555.
- [12] Xu, J., and Fisher, T. S., 2004, "Thermal Contact Conductance Using Carbon

- Nanotube Arrays,” in Proceedings of the 2004 ASME International Mechanical Engineering Congress and Exposition, Anaheim, CA, IMECE2004–60185, pp. 1–5.
- [13] Cruden, B. A., Cassell, A. M., Ye, Q., and Meyyappan, M., 2003, “Reactor Design Consideration in the Hot Filament/Direct Current Plasma Synthesis of Carbon Nanofibers,” *J. Appl. Phys.*, **94**, pp. 4070–4078.
- [14] Coleman, H. W., and Steele, W. G., 1999, *Experimentation and Uncertainty Analysis for Engineers*, Wiley, NY.
- [15] Brown, K. K., Coleman, H. W., and Steele, W. G., 1998, “A Methodology for Determining Experimental Uncertainties in Regressions,” *J. Fluids Eng.*, **120**, pp. 445–456.
- [16] Bahadur, V., Xu, J., Liu, Y., and Fisher, T. S., 2005, “Thermal Resistance of Nanowire-Plane Interfaces,” *J. Heat Transfer*, **127**, pp. 664–668.
- [17] McGee, G. R., Schankula, M. H., and Yovanovich, M. M., 1985, “Thermal Resistance of Cylinder-Flat Contacts: Theoretical Analysis and Experimental Verification of a Line-Contact Model,” *Nucl. Eng. Des.*, **86**, pp. 369–381.
- [18] Visser, J., 1989, “van der Waals and Other Cohesive Forces Affecting Powder Fluidization,” *Powder Technol.*, **58**, pp. 1–10.
- [19] Israelachvili, J. N., 1992, *Intermolecular and Surface Forces*, Academic, London, UK.
- [20] Bondi, A., 1964, “van der Waals and Other Cohesive Forces Affecting Powder Fluidization,” *Powder Technol.*, **58**, pp. 1–10.
- [21] Wexler, G., 1966, “The Size Effect and the Non-local Boltzmann Transport Equation in Orifice and Disk Geometry,” *Proc. Phys. Soc. London*, **89**, 927 (1966).
- [22] Touloukian, Y. S., and Buyco, E. H., 1970, *Thermophysical Properties of Matter*, Plenum, NY, Vol. 5.